https://doi.org/10.1016/j.ultrasmedbio.2020.09.024

ELSEVIER

● *Original Contribution*

TISSUE CHARACTERIZATION BY LOW-FREQUENCY ACOUSTIC WAVES GENERATED BY A SINGLE HIGH-FREQUENCY FOCUSED ULTRASOUND BEAM

GUILHERME A. BRAZ,* ANDRE L. BAGGIO,[†] PAULO M. AGNOLLITTO,[‡] FELIPE W. GRILLO,*
THEO Z. PAVAN,* FRANCISCO J.A. PAULA,[§] MARCELLO H. NOGUEIRA-BARBOSA,[‡]
GEORGE C. CARDOSO,* and ANTONIO A.O. CARNEIRO*

* Department of Physics, Faculty of Philosophy, Sciences and Letters, University of São Paulo, Ribeirão Preto, São Paulo, Brazil;
[†] Physics Institute, Federal University of Alagoas, Maceio, Brazil; [‡] Department of Medical Imaging, Hematology and Oncology,
Ribeirão Preto Medical School, University of São Paulo, Ribeirão Preto, São Paulo, Brazil; and [§] Department of Internal Medicine,
Ribeirão Preto Medical School, University of São Paulo, São Paulo, Brazil

Abstract—The mechanical properties of biological tissues are fingerprints of certain pathologic processes. Ultrasound systems have been used as a non-invasive technique to both induce kilohertz-frequency mechanical vibrations and detect waves resulting from interactions with biological structures. However, existing methodologies to produce kilohertz-frequency mechanical vibrations using ultrasound require the use of variable-frequency, dual-frequency and high-power systems. Here, we propose and demonstrate the use of bursts of megahertz- frequency acoustic radiation to observe kilohertz-frequency mechanical responses in biological tissues. Femoral bones were obtained from 10 healthy mice and 10 mice in which osteoporosis had been induced. The bones' porosity, trabecular number, trabecular spacing, connectivity and connectivity density were determined using micro-computed tomography (μCT). The samples were irradiated with short, focused acoustic radiation pulses (f = 3.1 MHz, t = 15 μs), and the low-frequency acoustic response (1−100 kHz) was acquired using a dedicated hydrophone. A strong correlation between the spectral maps of the acquired signals and the μCT data was found. In a subsequent evaluation, soft tissue stiffness measurements were performed with a gel wax-based tissue-mimicking phantom containing three spherical inclusions of the same type of gel but different densities and Young's moduli, yet with approximately the same echogenicity. Conventional B-mode ultrasound was unable to image the inclusions, while the novel technique proposed here showed good image contrast. (E-mail: adilton@usp.br) © 2020 World Federation for Ultrasound in Medicine & Biology. All rights reserved.

Key Words: Ultrasound, Radiation force, Mechanical properties, Tissue characterization, Osteoporosis, Elasticity.

INTRODUCTION

Acoustic radiation force (ARF) has been used to drive mechanical responses in biological tissue. Typical examples include measurement of mechanical properties (Urban 2018), manipulation of cells (Yongqiang et al. 2014), modulation of cellular behavior (Kamimura et al. 2016) and bio-effects investigations (Chandrasekaran et al. 2017). Benefits of these ARF methods of accessing the tissue include non-invasiveness, good localization of non-contact force with minimum disturbance to surrounding areas, easy modulation of the acoustic force and the development of technology

(Franchi-Abella et al. 2013). The use of dynamic ARF to excite the tissue enables low-frequency structural analysis (Nightingale et al. 2001; Nightingale 2011; Aristizabal et al. 2014; Dutta et al. 2015).

Low-frequency ultrasound probing of samples can be done with vibro-acoustography (Fatemi and Greenleaf 1999). This technique uses dynamic radiation forces generated by two ultrasound beams of slightly different frequencies focused on the same spatial location. The vibro-acoustographic response occurs at the primary ultrasound beams' frequency difference, which is low-frequency, usually two orders of magnitude below the original beams' frequencies. The low-frequency response carries the mechanical information of the portion of the tissue that the beams have interacted with (Alizad et al. 2004; Aguilo et al. 2010; Urban et al. 2011). The vibro-acoustography technique

Address correspondence to Antonio Adilton Oliveira Carneiro, Department of Physics, University of São Paulo, Av. Bandeirantes, 3900 Vila Monte Alegre, Ribeirão Preto, São Paulo, Brazil, 14049-900. E-mail: adilton@usp.br

has been explored to evaluate rigid tissues such as bones for the presence of fractures (Nogueira-Barbosa et al. 2017) and for total hip arthroplasty (Kamimura et al. 2013). The acoustic response (AR) in vibro-acoustography comes from the non-linear interaction of the ultrasound beam with the target (Silva 2010). Studies by Silva et al. (2007), Silva (2010), Silva and Mitri (2011) and Silva and Bandeira (2013) have shown that parametric effects arise when two acoustic waves of different frequencies interact in a non-linear acoustic medium. To optimize tissue response, one must use the optimal frequency difference. However, by working only with the optimal frequency, vibro-acoustography might miss important tissue spectral response information.

Here, we present a technique where a single pulse of focused ultrasound is used to excite a sample, which as a result produces a low-frequency broad-spectrum mechanical response that carries information about its mechanical structures. The high-frequency ultrasound pulse (MHz) helps us maintain a high resolution and preserves the directivity of the beam. This wave's interaction with the sample generates a broad spectrum of low frequencies (kHz), close to the natural resonance frequencies, through non-linear acoustic pulse propagation phenomena such as the self-demodulation effect proposed by Berktay (1965).

The goal of the present study is to demonstrate the technique proposed here for use in the mechanical characterization of biological tissue, showing the potential of the technique for characterizing soft and hard tissues of different stiffnesses and anatomies.

THEORY

The non-linear propagation of acoustic pulse waves gives rise to a phenomenon known as self-demodulation (Berktay 1965). Self-demodulation refers to the non-linear generation of a low-frequency AR caused by the interaction of a pulsed high-frequency acoustic beam with the sample. The self-demodulation phenomenon in sine envelope pulses has been shown to give rise to a single low-frequency component, similar to vibro-acoustography, but using only a focused beam (Vos et al. 2010; Daeichin et al. 2012; Kim et al. 2012). As demonstrated by Berktay (1965), the amplitude modulation of the carrier wave varies slowly relative to the center frequency of the pulse, the absorption length at the center frequency does not exceed the Rayleigh distance at that frequency and the process is non-linear, presenting no shock formation. The demodulated waveform predicted by Berktay (1965) is an extension of Westervelt's solution (Westervelt 1957) for the parametric array that is proportional to the second derivative of the square of the pulse envelope function $\partial^2 (E^2)/\partial t^2$. This analysis represents

a reasonable approximation, stating that a collimated primary wave of pressure $p_1(t) = P_1 E(t) \sin(\omega_c t)$, where P_1 is the amplitude of the primary beam pressure, $E(t)$ is the modulation envelope and ω_c is the carrier frequency, will demodulate, creating a secondary wave p_2 given in eqn (1) as

$$p_2(t) = C \frac{\partial^2 \left[E(t)^2 \right]}{\partial t^2} \tag{1}$$

where $C = \frac{A_c P_1^2 \beta}{16 \pi C_0^4 p 0 \alpha z}$, A_c is the beama cross-sectional area, β is the coefficient of non-linearity, z is the axial distance, α is the absorption coefficient of the medium (at frequency of ω_c), ρ_0 is the density of the medium and c_0 is the wave propagation speed.

Considering a Gaussian envelope $E(t) = A e^{-Bt}$ with $B = 1/(2\sigma^2)$, $A = 1$ for simplicity, eqn (1) can be written as

$$p_2(t) = C e^{-Bt2} \left(4B^2 t^2 - B \right) \tag{2}$$

In the frequency domain, eqn (1) and eqn (2) can be written as:

$$P_2(\omega) = \mathscr{F}\{p_2(t)\} = -C \frac{e^{-\frac{\omega^2}{8B}\omega^2}}{2\sqrt{B}} \tag{3}$$

The variance σ^2 is related to the full width at half maximum (FWHM) of the peak of the Gaussian envelope function $\left(FWHM/2\sigma \sqrt{(2In2)} \right)$. The signal detected by the hydrophone $Y(\omega)$ in frequency domain is function of the excitation pressure signal $P_2(\omega)$, the mechanical and AR of the system $W(R,\omega)$ and hydrophone transfer function sensitivity $H(\omega)$, as follows:

$$Y(\omega) = P_2(\omega) * W(R,\omega) * H(\omega) \tag{4}$$

The pressure $P_2(\omega)$ can be predicted from eqn (3).

Using this phenomenon, we propose a new technique, using localized high-frequency pulses to excite the tissue and low-frequency detection, with a dedicated hydrophone, to map the AR of the tissue under examination. The acquired ultrasound response has lower frequencies than those of the excitation beam and a wide frequency band, owing to the nature of the excitation. This scheme allows for a spectral analysis of the mechanical properties of the tissue while keeping the excitation pulse limited to a single frequency. We have named the proposed technique pulse emission acoustography (PEA).

MATERIALS AND METHODS

The experimental setup consisted of a focused ultrasonic excitation beam system emitting short pulses in the megahertz range and a calibrated

hydrophone acquisition system (International Transducer Corporation, ITC 6050 C, Santa Barbara, CA, USA; response band 0.300−100 kHz; average sensitivity of 157 dB/V/μPa). The excitation beam was generated by a focused ultrasound transducer produced in our laboratory, consisting of a concave piezoelectric ceramic (PZT4) with an aperture of 20 mm, resonance frequency at 3.16 MHz, bandwidth of 24 kHz (3.04−3.28 MHz), focal distance of 50 mm and driven by a waveform function generator (Agilent 33220 A, Santa Clara, CA, USA) configured in burst mode, amplified by a dedicated power amplifier to deliver up to 100 Vpp excitation. A MATLAB (MATLAB Release 2012b, The MathWorks, Inc., Natick, MA, USA) algorithm generated the excitation wave pattern, which was stored in the function generator memory *via* USB protocol. The acoustic pressure in the focal point of the transducer was 1.9 MPa. A scheme of the experimental setup can be seen in Figure 1. The excitation pattern was a sinusoidal wave with a central frequency of 3.16 MHz, modulated by a Gaussian function to produce a low-frequency band on account of the self-demodulation effect.

The AR was processed using an algorithm written in MATLAB (MATLAB and Statistics Toolbox Release 2012b, The MathWorks, Inc., Natick, MA, USA). The first step was to window the acquired signal to select the region of interest, and to Fourier transform the windowed signal from the obtained power spectrum, the properties of the irradiated sample were correlated to the amplitude at a suitable frequency of interest.

To produce images using this technique, we defined a transverse x-y plane orthogonal to the axial direction of the focused beam. The focus of the excitation transducer was then positioned at each point P (x, y). A prismatic three-axis robot was used to move the transducer (or the sample) along the x-y plane, parallel to the ultrasonic excitation beam. For each of these points, an AR signal was obtained and associated with the value of a pixel in the image. In order to evaluate AR contrast with

the technique, an experiment was performed using a metal sphere of 1 mm diameter in water, suspended by a thin nylon mount as a target. Figure 2 shows the metal sphere positioned in the focal point of the ultrasound transducer. The ultrasound beam was focused on the location of the sphere. The experiment was repeated ten times (with and without the sphere) to obtain the average AR for each of the two cases. After that, the Fourier transforms of the averaged signals were obtained.

PEA setup for osteoporosis diagnosis

This study was conducted using mouse femora obtained from a previous experimental study conducted at our laboratory and approved by the Institutional Animal Care and Use Committee of the Ribeirão Preto Medical School, University of São Paulo (protocol no. 111/2011). New committee approval was waived because no new animal experiment was necessary.

Study design and animals

In those experiments, 5-wk-old mice weighing approximately 18 g were used. The animals were maintained in cages in a room with controlled humidity and temperature (23 ± 1 °C), and with an artificial light/dark cycle of 12 h (lights on: 6:00 AM to 6:00 PM). The animals had free access to tap water and pellet chow.

Two groups of mouse femora were prepared (control and osteoporotic). The control group contained 10 healthy specimens. The other group was composed of 10 specimens submitted to an intraperitoneal injection of CCl_4 (1 mL/kg weight) dissolved in olive oil 1:4 (v:v), which induces hepatic disease, leading to the development of osteoporosis (Klein et al. 2002). The femoral bone from the right leg of each individual animal was removed to be used as a sample. The head of the femur with the overlying soft tissues removed was used as a target. Each bone was placed in the focal point of the ultrasound transducer. The hydrophone was placed 5 cm to the side of the ultrasound transducer. The samples were irradiated by
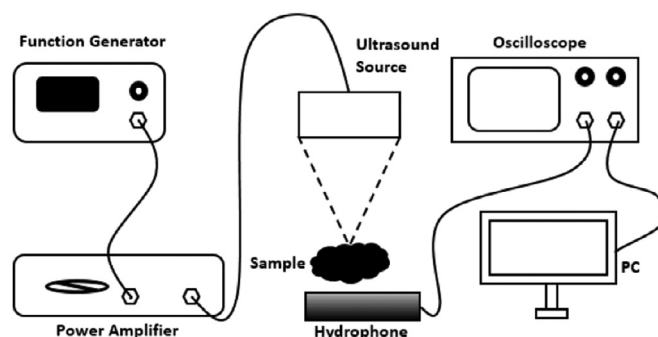

Fig. 1. Experimental setup: A function generator creates a burst mode signal pattern that is amplified to drive an ultrasound focused transducer. A calibrated hydrophone detects the acoustic response signal and sends it to an oscilloscope linked to a computer to be processed.
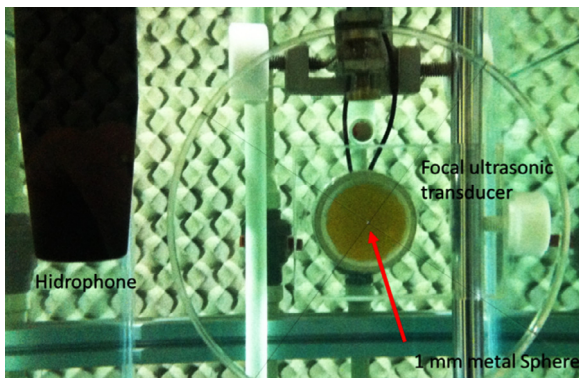
Fig. 2. Image of the experimental setup showing the arrangement of the focused transducer, the hydrophone and a target (metallic sphere) placed in the focus of the transducer.
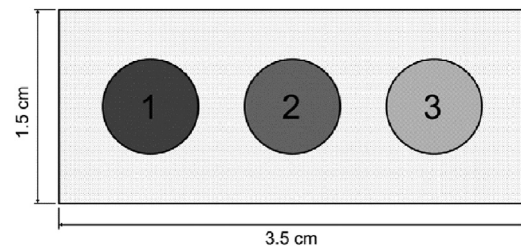

Fig. 3. Morphology of the phantom and inclusions distribution. The background and inclusions were made of gel wax, with different stiffnesses. Inclusions 1, 2 and 3 have Young's Moduli of 98 kPa, 27 kPa and 18 kPa, respectively.

ultrasound pulses, and an AR signal was acquired for each of them. An analysis of variance (ANOVA) of the PEA signals from each of the two groups was done to study the significance of the difference between the signals coming from healthy and osteoporotic bones. As a reference technique to evaluate bone properties and estimate their correlation with the AR signals, a μCT (1172; SkyScan, Kontich, Belgium) was performed in the distal portion of the femoral bone, starting at 0.25 mm proximal to the distal growth plate and covering a total length of 1 mm. The CT-analyzer software (version 1.13.2.1) was used for quantitative assessment. The parameters acquired by the μCT were the as follows: bone volume fraction (BV/TV), which is the ratio of the segmented bone volume (BV) by the total volume (TV) of the region of interest; trabecular number (Tb.N), which is the measure of the average number of trabeculae per unit length; trabecular thickness (Tb.Th), which is the mean thickness of trabeculae; trabecular spacing (Tb.Sp), which is the mean distance between trabeculae; connectivity (Conn), which is the connectivity of trabeculae; and connectivity density (Conn.D), which is a measure of the degree of connectivity of trabeculae normalized by TV (Bouxsein et al. 2010). A Spearman correlation test was applied to evaluate the correlation between the AR and the μCT parameters. The statistical analysis was performed using R software (R: A language and environment for statistical computing. R Foundation for Statistical Computing, Vienna, Austria). A *p* value of less than 0.05 was considered statistically significant.

PEA setup for the imaging of a soft tissue−mimicking phantom with inclusion

To test the capability of the technique to generate images of soft tissue and distinguish tissues of different stiffnesses, a tissue-mimicking phantom was developed to emulate the acoustical and mechanical properties of soft tissues. This tissue-mimicking phantom was made

using high-density gel wax (Gel Candle, Ribeirão Preto Brazil) and low-density gel wax (Gel Candle, Ribeirão Preto, Brazil). Aiming to have three different stiffnesses with similar acoustic impedance, both gel wax types were mixed in the same proportion. Thus, three spherical inclusions were prepared: low-density gel, high-density gel and a mix of the two. In preparation for the spherical inclusion, the materials were heated for 6 h in an oven at 160žC and poured into a metallic mold, where they cooled down. Figure 3 shows the morphology of the phantom inclusions and their respective Young's moduli (Cabrelli et al. 2017; Grillo et al. 2018). With the same echogenicity, these inclusions would not appear in a conventional B-mode image. The purpose of this experiment was to show that the PEA technique was able to image the isoechoic inclusions as well.

The isoechoic inclusions had their Young's moduli measured by mechanical compression using a Ta.Xt Plus (Stable Micro Systems, Godalming, UK) texturometer with a probe of 40 mm in diameter. The phantom with inclusions was imaged both with the PEA technique and with conventional B-mode imaging. The size of the scanned region was 1.5 cm × 3.5 cm, with a spatial resolution of 0.25 mm. A region of interest was chosen in the PEA image for each of the three inclusions, with a window of 3 × 3 mm, and a box plot of the AR values from each inclusion was made to show the dependency of the signal with the stiffness variation. A correlation test was performed between the signals from each inclusion and the young's moduli measured in the mechanical test.

RESULTS

Figure 4 shows the excitation signal profile containing a carrier frequency at 3.16 MHz modulated by a Gaussian envelope function. Figure 5 shows two normalized curves in the frequency domain. The dashed line shows the result of the self-demodulation effect when we applied the spindle parameters shown in eqn (3), indicating a low-frequency response ranging from 30−110 kHz. The solid line shows the detector (hydrophone) sensitivity
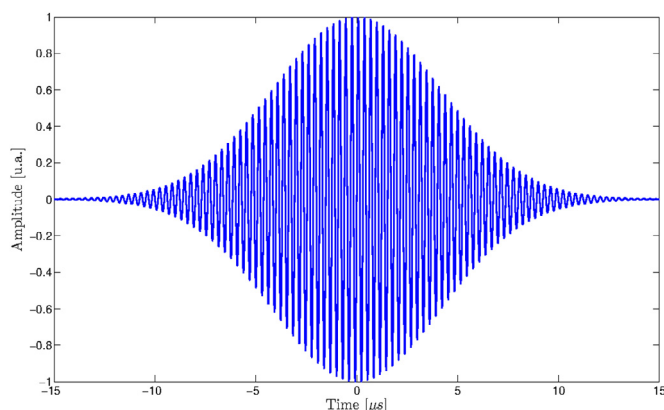
Fig. 4. Excitation signal pattern: A 3.25 MHZ sine wave modulated by a Gaussian envelope.
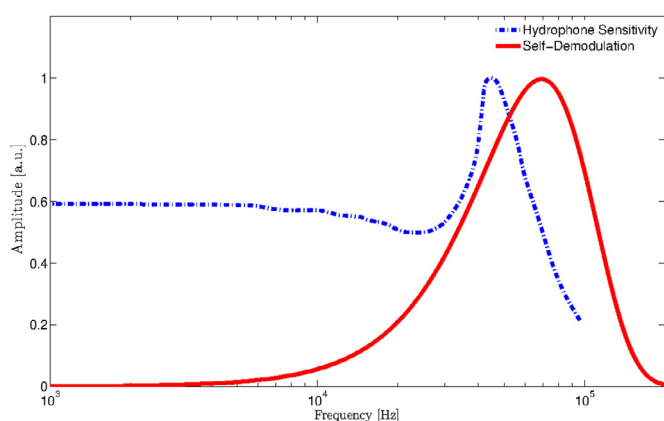

Fig. 5. System spectral response. (a) The dashed line represents hydrophone detector sensitivity (normalized), and the solid line is the self-demodulation spectrum obtained from eqn (3). The Gaussian parameter is related to the full width at half maximum (FWHM) of the peak of the Gaussian envelope function ($= FWHM/2\sqrt{2ln2}$).

obtained from the manufacturer's calibration curve, showing that the chosen detector is able to detect the AR.

Figure 6 shows the AR results with and without the 1.0 mm metal sphere at the focal region of the excitation wave, as described earlier. The AR amplitude difference between the two cases is very distinctive, showing that PEA is sensitive enough to detect the small scattering object. The contribution of the sphere on the signal starts at 77 μs. This is the time it takes for the pulse leaving the ultrasound transducer to interact with the sphere and the AR to arrive at the hydrophone.

The Fourier transform of the signals presented in Figure 6 is shown in Figure 7. The difference in both the amplitude and frequency of the main spectral peaks confirm good contrast between the cases with and without the metal sphere in the focal region of the ultrasound transducer. The experiment also shows that contrast can be obtained by using either the difference in the amplitude of the low-frequency AR signal from the sample or AR spectral analysis.

Results of the application of the PEA technique in bone characterization

Results of PEA AR values for both control and osteoporotic bones are shown in Table 1. The PEA AR values were normalized to peak intensity. Figure 8 is a representation of the AR results from Table 1 as box plots. The ANOVA test determined excellent discrimination between the two groups ($p < 0.01$), suggesting that PEA has potential for osteoporosis diagnosis.

Figure 9 shows the plot of each of the μCT parameters versus normalized AR for each bone from the control and osteoporotic groups. Table 2 displays the Spearman correlations between those variables. Results show PEA AR has a strong correlation with the trabecular number (Tb.N) and a moderate one with trabecular spacing (Tb.Sp), connectivity (Conn) and connectivity density (Conn.D).

Figure 10a shows the results of an additional experiment where PEA AR was used to image a rat femoral bone; a photograph can be seen in Figure 10b. This result shows that the technique is suitable to image bone tissue.
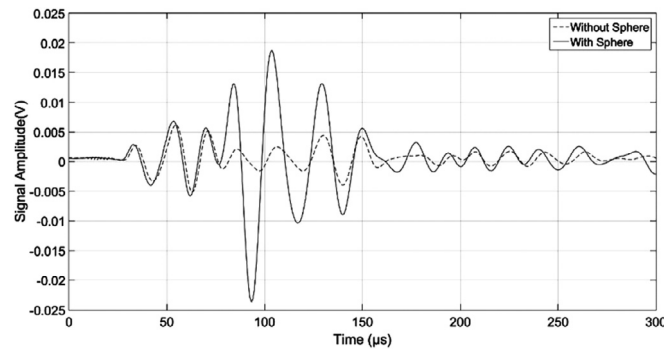
Fig. 6. Differences between the signals obtained with (*solid line*) and without (*dashed line*) a metal sphere in the focal region of the transducer.
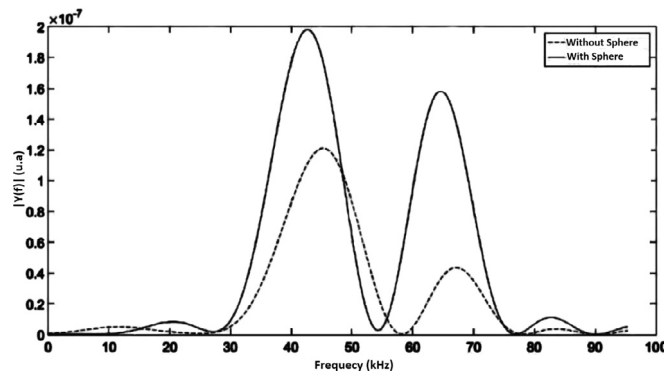

Fig. 7. Fourier transform of the signals from Figure 6 with (*solid line*) and without (*dashed line*) a metal sphere into the focal point.

Table 1. Normalized acoustic response value obtained using the acoustic radiation force

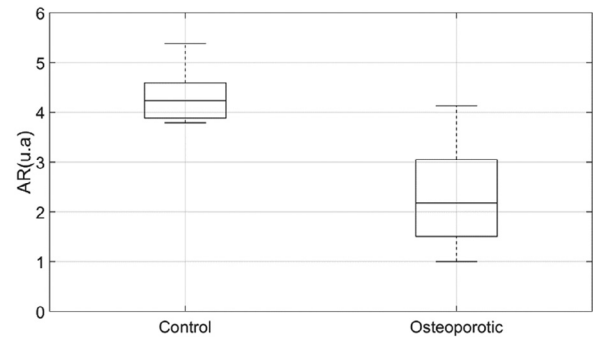| Control	Osteoporotic
5.38	4.13
4.78	3.53
4.59	3.05
4.46	2.76
4.42	2.44
4.05	1.91
3.96	1.52
3.88	1.51
3.84	1.21
3.79	1.00

Fig. 8. Box plot of the acoustic response (AR) results from the control and osteoporotic groups shown in Table 1.

The generated image has a well-defined border, is free of speckles and presents high contrast.

PEA results for soft tissue−mimicking phantoms with inclusions

In Figure 11, we can see the PEA AR−generated image and B-mode image of the tissue-mimicking phantom. The image obtained by the novel PEA AR technique proposed here shows good contrast in the region of the inclusions, while the B-mode image is unable to produce enough contrast to identify the inclusions in the phantom base material, showing that the new technique brings new information compared with conventional ultrasound. Figure 12 shows the box plot of AR results from each inclusion. Young's modulus versus the average AR value for these inclusions is shown on Table 3, where the AR values were obtained from an ROI (3 × 3 mm) in the region of the
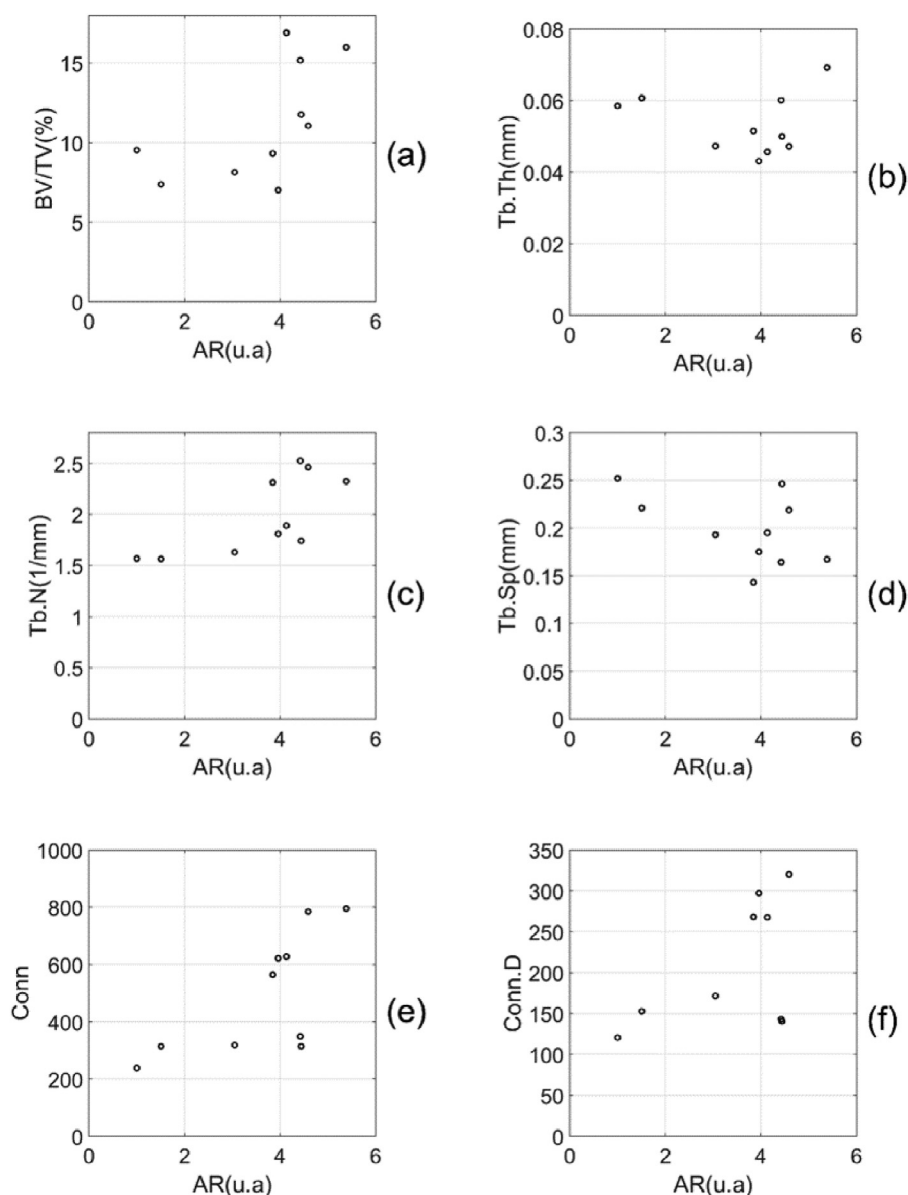
Fig. 9. Acoustic response (AR) signal of each bone versus the μCT parameters. (a) AR versus BV/TV;(b) AR versus Tb. Th; (c) AR versus Tb.N; (d) AR versus Tb.Sp; (e) AR versus Conn; (f) AR versus Conn.D. BV/TV = bone volume/total volume; Conn = connectivity; Conn.D = connectivity density; Tb.N = trabecular number; Tb.Sp = trabecular spacing; Tb. Th = trabecular thickness.

Table 2. Results of Spearman correlation tests between the μCT parameters and the AR signal

μCT parameter versus AR	Spearman Correlation (p)	p Value
BV/TV(%)	0.6 0	0.0 69
Tb.Th(mm)	−0.08	0.819
Tb.N(l/mm)	0.72	0.020
Tb.Sp(mm)	−0.51	0.136
Conn	0.69	0.026
Conn.D	0.64	0.044

inclusions from Figure 11a. The Spearman correlation test between the PEA AR averaged signals and the mechanical test signals found a value of r = 0.94, showing a strong correlation between the PEA AR signal and the Young's modulus of each inclusion.

DISCUSSION

In this study, we propose a new ultrasound technique—PEA —that uses high-power, pulsed, single-frequency, focused ultrasound, and we use this technique to

characterize ex vivo bone samples (for osteoporosis diagnosis) and soft tissue phantom simulators.

The self-demodulation theory estimated a low-frequency response from the samples, with a frequency band between 30 and 110 kHz, as observed in Figure 5. This prediction matches the measured spectrum from the hydrophone signals in the metal sphere experiment (Fig. 7). It is possible to observe a frequency shift in the peak values, leading us to believe that there was a distortion in the shape of the envelope function as it interacted with the sphere, changing the effect of the self-demodulation. The consequence of these two modifications is that the difference between the two signals, either in peak amplitude or displacement in the resonance peak frequency value, produced a reasonable contrast between the presence and absence of the metallic spherical inclusion. It is important to notice that there is a difference between the theoretic curves and the measured spectrum; this occurs because the estimated curve does not take into account geometry and scattering factors, and we still cannot fully predict the behavior of the acquired signal depending on the mechanical and geometric characteristics of the sample. The dependence of the PEA spectral signal with the mechanical and morphologic properties of the sample is still unknown and is currently under investigation.

We would like to highlight potential uses of the PEA technique in bone characterization, especially for osteoporosis diagnosis. The results shown in Figure 8, together with the ANOVA test, show that PEA can detect differences between healthy and osteoporotic bones. The results shown in Table 3 gives us some of the mechanical parameters (measured by the μCT) to which the technique is sensitive, namely trabecular number (Tb.N) and trabecular spacing (Tb.Sp), both related to bone porosity. A strong correlation was obtained with the trabecular number (Spearman correlation coefficient of 0.72 and *p* value of 0.02). Also, a moderate correlation has been found with the connectivity (Conn) and connective density (Conn.D) parameters (Spearman correlation coefficients of 0.69 and 0.64 and *p* values of 0.03 and 0.04), showing that the technique is sensitive to the mechanical parameters that change between the samples. No correlation was observed between the trabecular thickness (Tb.Th) μCT parameter and AR, because no difference was observed for this μCT parameter between the osteoporotic and control groups.

The image of the mouse femoral bone in Figure 10 presents a high spatial resolution, compatible with the frequency diffraction limit of 3.16 MHz, and it has a sharp appearance, well-defined contours and no speckles, reverberations or other artifacts inherent to a conventional ultrasound image. This imaging technique (PEA) is able to identify a concave region present in the femoral bone, something that would be difficult to observe using B-mode ultrasound imaging. It should be noted, however, that some parts of the femoral head did not appear on the PEA image. This is explained by two reasons: First, the high axial resolution of the focused high-frequency beam means that the parts of the bone that are not in the x-y plane of the image are not displayed; secondly, the missing part in the image corresponds to cartilaginous tissue, which has significantly different mechanical properties from bone. PEA presents a clear advantage over traditional single-frequency vibro-acoustography, which requires re-imaging at a new frequency to observe the missing tissue. The broad spectrum of PEA AR signals allows the production of images at multiple frequencies from the same collected data, allowing a complete spectral analysis of the different points of the sample.
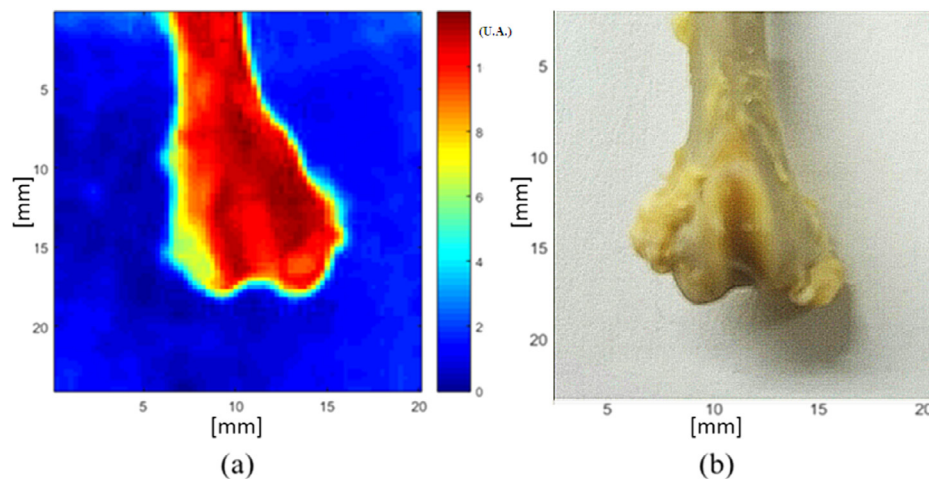

Fig. 10. (a) Image of the rat femoral bone obtained using pulse emission acoustography (PEA) acoustic response (AR); (b) photography of the same bone sample in the same imaged area.
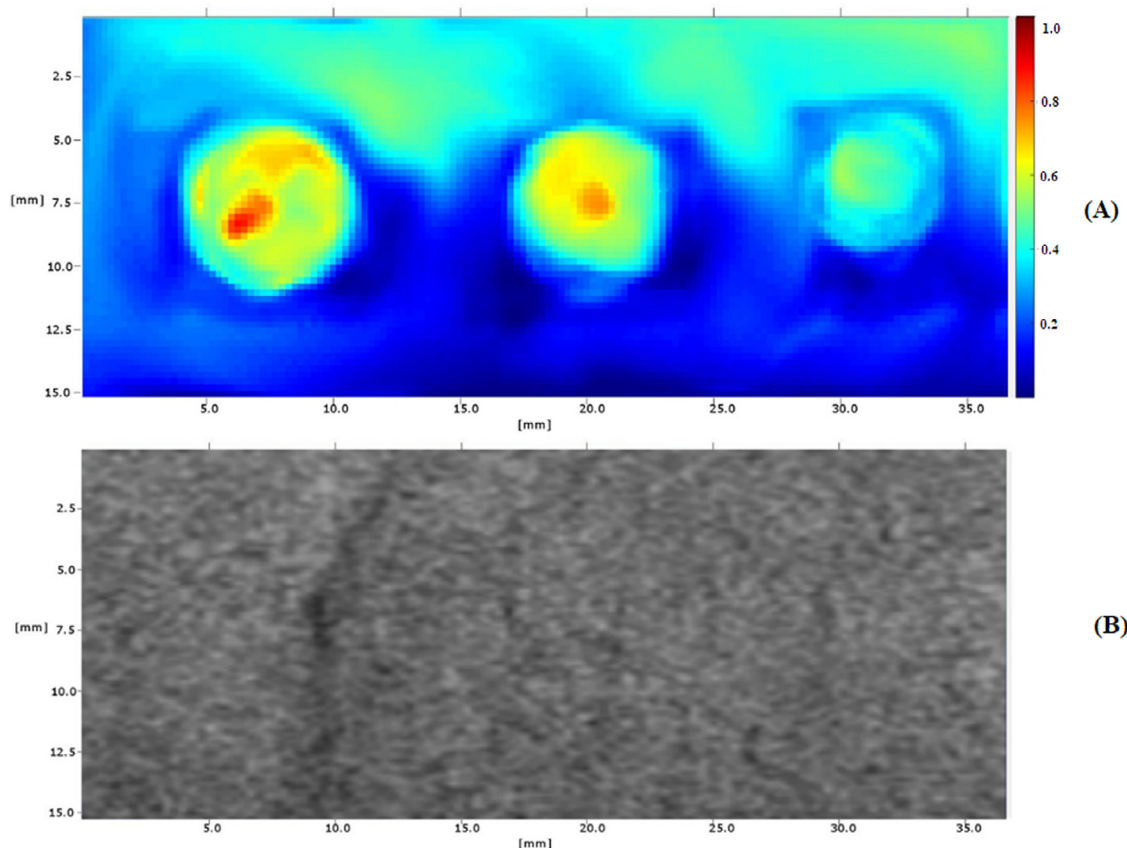
Fig. 11. (a) Soft tissue−mimicking phantom image produced using the pulse emission acoustography (PEA) acoustic response (AR)-proposed technique. Gel wax of different density was used to mimic the background and inclusion material of this phantom (see Fig. 5); (b) : B-mode image of the same phantom.
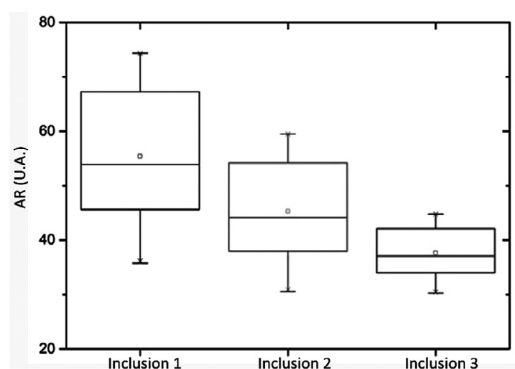

Fig. 12. Box plot generated from the pulse emission acoustography (PEA) acoustic response (AR) signals extracted from a Region of Interest in each of the three inclusions.

In the PEA technique, despite the use of ARF impulse (ARFI), the physical principle involved in the interaction of the ultrasound wave pulse with the target, as well as the mechanisms to record the PEA signal, is categorically different from all other elastography techniques. For example, typical shear wave elastography images based on ARFI apply a long ultrasound pulse in the order of 1 ms to induce a shear wave in the region of interest. Along with pressure pulses, pulse-echo ultrasound beams are continuously emitted using the same ultrasound transducer to monitor tissue displacement. From such data, the velocities of the shear waves and tissue stiffness are obtained. Thus, shear wave elastography assumes that a stiffer medium would deform less than a softer one. On the other hand, the PEA AR assumes that differences in the mechanical structure and morphology of the excited regions will modify the low-frequency component of the scattered ultrasound wave. Yet, as in shear wave elastography, PEA imaging also produces soft-tissue images with good contrast between regions of different stiffnesses.

Referring back to the theory of self-demodulation, constant C of eqn (1) takes into account medium parameters such as density, sound speed and non-linear coefficient. This fact provides a reasonable contrast in situations where echogenicity is maintained in different tissues but has differences in density (sometimes caused by disease). B-mode images would not be sensitive to

Table 3. The Young's modulus versus the average value of AR response of the inclusions

Inclusion	Average PEA AR (u.a)	Young's moduli (kPa)
1	55 ± 11	98 ± 1
2	45 ± 8	27 ± 1
3	37 ± 4	18 ± 1

AR = acoustic response; PEA = pulse emission acoustography.

this type of change because scatter patterns would not offer significant contrast. Figure 11 shows a gel phantom that was subject to both PEA imaging and B-mode ultrasound imaging. Conventional B-mode ultrasound images do not allow for the identification of the inclusions, because although their Young's moduli are higher than that of the surrounding background, they have the same echogenic properties as the surrounding material. However, using the PEA technique, the inclusions could be detected, as shown in the color map, indicating that PEA is sensitive to stiffness changes. From the images of the soft tissue−mimicking phantom, it can be seen that PEA has the potential to identify and characterize harder portions or inclusions in tissues. The fact that the inclusions in the phantom do not appear in the B-mode image, yet are very clear in the PEA image, highlights the high potential of applications of the PEA technique compared with conventional ultrasound techniques. Although it has shown good potential to differentiate stiffness within the phantom, this acoustic technique cannot be considered quantitative.

Mechanical tests were performed on tissue-mimicking phantom inclusions and compared with contrast by the PEA technique. The good correlation obtained between the values of AR and Young's modulus ($r = 0.94$) demonstrated the potential of this proposed technique to also map small differences in stiffness in soft tissues.

As a further advantage, images generated using the proposed PEA technique, based on ARF, are free from speckles because of the low frequencies of the AR used in the image formation. The low directivity of the emitted acoustic signal helps in the formation of images of objects with irregular surfaces, like bones. Also, with just one acquisition, it is possible to do a multi-frequency analysis.

Challenges in the PEA technique include engineering the excitation envelope to optimize low-frequency band production and understanding the importance of other non-linear beam propagation phenomena, as well as the interaction between the ARF and the mechanical properties of the beam. Further investigation, as well as additional data, is required to ensure that the PEA technique is a good option to characterize biological tissue. Future studies will test the suitability of the PEA technique for in vivo tissue characterization.

CONCLUSIONS

This study presents a new technique called PEA that is able to differentiate changes in the mechanical properties of rigid and soft tissues. Based on the non-linear acoustic beam propagation phenomenon called self-demodulation, this novel technique was shown to be able to produce low frequencies of the order of kilohertz from a focused high-frequency (MHz) ultrasonic beam. In the AR signal obtained with and without a metal sphere, PEA showed not only the existence of low-frequency signals following the theory of self-demodulation, but also significant contrast in both amplitude and frequency shifts. The experiment with a soft tissue simulator showed that the PEA was efficient in detecting stiffness changes in inclusions with echogenicity equal to the surrounding medium, as opposed to a B-mode image that failed to detect the inclusions. In hard tissue, the technique succeeded in imaging a rat femoral bone, highlighting morphologic concavities and different tissues. The statistical tests have shown efficiency in discriminating healthy from osteoporotic tissue. The central advantage of the technique is that by producing an excitation modulated by a low-frequency envelope, it enables the activation of different vibrational modes, and by scattering in different biological tissue structures, it allows a spectroscopic analysis of a sample, as well as better tissue suppression in images.

Conflict of interest disclosure—The authors declare that they have no conflicts of interest.

REFERENCES

Aguilo M, Aquino W, Brigham J, Fatemi M. An inverse problem approach for elasticity imaging through vibroacoustics. IEEE Trans Med Imaging 2010;29:1012–1021.

Alizad A, Wold L, Greenleaf J, Fatemi M. Imaging mass lesions by vibro-acoustography: Modeling and experiments. IEEE Trans Med Imaging 2004;23:1087–1093.

Aristizabal S, Amador C, Qiang B, Nenadic IZ, Greenleaf JF, Urban MW. Viscoelastic characterization of transverse isotropic tissue mimicking phantoms and muscle. *2014 IEEE International Ultrasonics Symposium*. Chicago, IL: IEEE; 2014. p. 228–231. doi: 10.1109/ULTSYM.2014.0058.

Berktay H. Possible exploitation of non-linear acoustics in underwater transmitting applications. J Sound Vibrat 1965;2:435–461.

Bouxsein ML, Boyd SK, Christiansen BA, Guldberg RE, Jepsen KJ, Müller R. Guidelines for assessment of bone microstructure in rodents using micro-computed tomography. J Bone Miner Res 2010;25:1468–1486.

Cabrelli LC, Pelissari PIBGB, Deana AM, Carneiro AAO, Pavan TZ. Stable phantom materials for ultrasound and optical imaging. Phys Med Biol 2017;62:432–447.

Chandrasekaran SN, Holm S, Prieur F. Focused ultrasound setup for the study of acoustic radiation force induced biological effects in

cells. 2017 IEEE International Ultrasonics Symposium. Washington, DC1–4.

Daeichin V, Needles A, Skachkov I, Kooiman K, Bosch J, van der Steen A, de Jong N. Optimized high frequency nonlinear contrast imaging using self-demodulation. *2012 IEEE International Ultrasonics Symposium*. Dresden: IEEE; 2012. p. 1110–1113. doi: 10.1109/ULTSYM.2012.0276.

Dutta P, Urban MW, Maitre OPL, Greenleaf JF, Aquino W. Simultaneous identification of elastic properties, thickness, and diameter of arteries excited with ultrasound radiation force. Phys Med Biol 2015;60:5279–5296.

Fatemi M, Greenleaf JF. Vibro-acoustography: An imaging modality based on ultrasound-stimulated acoustic emission. Proc Natl Acad Sci U S A 1999;96:6603–6608.

Franchi-Abella S, Elie C, Correas JM. Ultrasound elastography: Advantages, limitations and artefacts of the different techniques from a study on a phantom. Diagn Interv Imaging 2013;94:497–501.

Grillo FW, Souza VH, Matsuda RH, Rondinoni C, Pavan TZ, Baffa O, Machado HR, Carneiro AAO. Patient-specific neurosurgical phantom: Assessment of visual quality, accuracy, and scaling effects. 3D Print Med 2018;4(3).

Kamimura H, Wang L, Carneiro A, Kinnick R, An K, Fatemi M. Vibroacoustography for the assessment of total hip arthroplasty. Clinics 2013;68:463–468.

Kamimura HAS, Wang S, Chen H, Wang Q, Aurup C, Acosta C, Carneiro AAO, Konofagou E. Focused ultrasound neuromodulation of cortical and subcortical brain structures using 1.9 MHz. Med Phys 2016;43:5730–5735.

Klein GL, Soriano H, Shulman RJ, Levy M, Jones G, Langman CB. Hepatic osteodystrophy in chronic cholestasis: Evidence for a multifactorial etiology. Ped Transplant 2002;136–140.

Kim SE, Hwang JH, Kang TW, Kang SW, Sohn SW. Generation of audible sound with ultrasonic signals through the human body. *2012 IEEE 16th International Symposium on Consumer Electronics*. Harrisburg, PA: IEEE; 2012. p. 1–3. doi: 10.1109/ISCE.2012.6241713.

Nightingale K. Acoustic radiation force impulse (ARFI) imaging: A review. Curr Med Imag Rev 2011;7:328–339.

Nightingale KR, Palmeri ML, Nightingale RW, Trahey GE. On the feasibility of remote palpation using acoustic radiation force. J Acoust Soc Am 2001;110:625–634.

Nogueira-Barbosa MH, Kamimura HAS, Braz G, Agnollitto PM, Carneiro AAO. Preliminary results of vibro-acoustography evaluation of bone surface and bone fracture. Quant Imaging Med Surg 2017;7:549–554.

Silva GT. Dynamic radiation force of acoustic waves on absorbing spheres. Braz J Phys 2010;40.

Silva GT, Bandeira A. Difference-frequency generation in nonlinear scattering of acoustic waves by a rigid sphere. Ultrasonics 2013;53:470–478.

Silva GT, Mitri FG. Difference-frequency generation in vibro-acoustography. Phys Med Biol 2011;56:5985–5993.

Silva GT, Urban MW, Fatemi M. Multifrequency radiation force of acoustic waves in fluids. Physica D: Nonlinear Phenomena 2007;232:48–53.

Urban MW, Alizad A, Aquino W, Greenleaf JF, Fatemi M. A review of vibro-acoustography and its applications in medicine. Curr Med Imaging Rev 2011;7:350–359.

Urban MW. Production of acoustic radiation force using ultrasound: Methods and applications. Expert Rev Med Devices 2018;15:819–834.

Vos HJ, Goertz DE, de Jong N. Self-demodulation of high-frequency ultrasound. J Acoust Soc Am 2010;127:1208–1217.

Westervelt PJ. Scattering of sound by sound. J Acoust Soc Am 1957;29:199–203.

Yongqiang Q, Wang H, Demore C, Hughes D, Glynne-Jones P, Gebhardt S, Bolhovitins A, Poltarjonoks R, Weijer K, SchAunecker A, Hill M, Cochran S. Acoustic devices for particle and cell manipulation and sensing. Sensors 2014;14:14806–14838.